PAPER

Check for updates

A new spinel high-entropy oxide $(Mg_{0.2}Ti_{0.2}Zn_{0.2}Cu_{0.2}Fe_{0.2})_3O_4$ with fast reaction kinetics and excellent stability as an anode material for lithium ion batteries†

Hong Chen, [iD] Nan Qiu, [iD]* Baozhen Wu, Zhaoming Yang, Sen Sun and Yuan Wang*

It is well known that transition metal oxides (TMOs) have attracted extensive attention as promising anodes for next-generation lithium ion batteries (LIBs) owing to their low cost and high theoretical capacities. However, the huge volume changes upon lithiation/delithiation cycling gradually cause drastic particle pulverization in the electrodes, thus leading to fast capacity fading and limiting their practical applications. High-entropy oxides with enhanced electronic conductivity and multiple electrochemically active elements display stepwise lithium storage behaviors, thus efficiently alleviating the volume change induced electrode pulverization problem. Herein, we report the synthesis of a new kind of spinel $(Mg_{0.2}Ti_{0.2}Zn_{0.2}Cu_{0.2}Fe_{0.2})_3O_4$ material *via* a facile one-step solid state reaction method and subsequent high-energy ball-milling. When used as anodes for LIBs, the submicrometer-sized $(Mg_{0.2}Ti_{0.2}Zn_{0.2}Cu_{0.2}Fe_{0.2})_3O_4$ particles exhibit superior lithium storage properties, delivering a large reversible capacity of 504 mA h g^{-1} at a current density of 100 mA g^{-1} after 300 cycles, and notably an exceptional rate capacity of 272 mA h g^{-1} at 2000 mA g^{-1}. Our work highlights that rational design of high-entropy oxides with different electrochemically active elements and novel structures might be a useful strategy for exploring high-performance LIB anode materials in next-generation energy storage devices.

1. Introduction

Due to the ever-increasing energy demands and concern around global warming, advanced renewable energy technologies such as portable electronics, electric vehicles and green grid energy storage, have received much attention.[1–5] To satisfy the growing demand of advanced rechargeable lithium-ion batteries (LIBs), tremendous efforts have been devoted to explore the electrode materials with long cycle lives, high rates and reversible specific capacities.[6–8] Graphite is a commonly used anode material in current commercial LIBs.[9] Nevertheless, its low theoretical capacity (372 mA h g^{-1}) and the problem of Li dendrite formation limits the large-scale application in future LIBs system.[10,11] Therefore, developing suitable anode materials with higher lithium storage capacities and superior cycle stability is urgently demanded.[12–14] As promising anodes for LIBs, transition metal oxides (TMOs, such as Co_3O_4,[15] ZnO,[16] CuO,[17–21] Fe_3O_4,[22–25] Fe_2O_3 (ref. 25–27)) have attracted extensive attention owing to their low-cost and high theoretical capacities.

However, the large volume changes upon the lithiation/delithiation process gradually causes drastic electrode pulverization, thus leading to fast capacity fading.[3,28,29]

In order to solve the pulverization problem and to achieve enhanced cycling stability, it is reported that introducing foreign atoms into the single metal oxides could be a predominant effective method. A wide variety of ternary oxides have been studied as prospective anode materials for Li-ion batteries which undergo Li-cycling *via* the "conversion reaction," and those have been recently reviewed by Reddy *et al.*[12,25,30–37] In particular, iron-based spinel oxides, such as ferrites with general formula AFe_2O_4 (A = Zn, Ni, Co, Cu, Cd)[38–40] and $(Ni_{1-x}Zn_x)Fe_2O_4$ ($x = 0, 0.2, 0.25, 0.4, 0.5, 0.6, 0.75, 0.8, 1$)[41,42] have been extensively studied for their Li-cyclability. Specifically, Zhao and Luo *et al.*[43–45] suggested that the *in situ* formed Cu nanoclusters from $CuFe_2O_4$ not only promoted the reversible formation and decomposition of Li_2O but also functioned as an excellent buffer matrix for the Fe_2O_3 electrode, preventing the aggregation of Fe nanograins and buffering volume changes and structural stress of the electrode during cycling. Thus, excellent electrochemical performance was achieved in the composite $CuFe_2O_4$ electrode. Meanwhile, another effective method was complexing with electrochemically inactive materials such as MgO and CaO, which can cause a "spectator effect"

Key Laboratory of Radiation Physics and Technology, Ministry of Education, Institute of Nuclear Science and Technology, Sichuan University, Chengdu 610064, People's Republic of China. E-mail: qiun@scu.edu.cn; wyuan@scu.edu.cn

to restrain the agglomeration of active nanograins.[46–52] Therefore, more efforts and rational design strategies must be done to exploit suitable TMO anode materials with good cycling stability and high specific capacity, which will satisfy practical applications.

High-entropy oxides (HEOs), as a new kind of multicomponent and single-phase solid solution TMOs, have greater electronic conductivity and multiple electrochemically active components as compared with single metal oxides.[53–58] They display stepwise lithium storage behaviors, thus efficiently alleviating the volume change and then solving induced electrode pulverization problem to some extent. Herein, we have successfully synthesized a new spinel-structured $(Mg_{0.2}Ti_{0.2}Zn_{0.2}Cu_{0.2}Fe_{0.2})_3O_4$ materials *via* a facile one-step solid state reaction method and subsequently high-energy ball-milling. When used as anodes for LIBs, the $(Mg_{0.2}Ti_{0.2}Zn_{0.2}Cu_{0.2}Fe_{0.2})_3$-$O_4$ electrode exhibits superior lithium storage properties, delivering a large reversible capacity of 504 mA h g^{-1} at a current density of 100 mA g^{-1} after 300 cycles, and notably an exceptional rate capacity of 272 mA h g^{-1} at 2000 mA g^{-1}. Meanwhile, a high capacity retention of 96.2% after 800 cycles at 2000 mA g^{-1} was obtained.

2. Experimental section

2.1. Materials synthesis

All chemical reagents (purchased from Alfa Aesar Chemical Reagent Co., Ltd) were of analytical purity and used without any further purification. Equimolar amounts of the oxides, MgO (0.01 mol, 0.4030 g, 99.99%), TiO_2 (0.01 mol, 0.7987 g, 99%), FeO (0.01 mol, 0.7184 g, 99%), ZnO (0.01 mol, 0.8139 g, 99.9%) and CuO (0.01 mol, 0.7954 g, 99.9%) were mixed as pre-alloyed powder by a planetary ball mill. To ensure adequate mixing, all pre-alloyed powder was milled for at least 2 hours. The mixed powder was then separated into several samples with a weight of 0.500 g per sample, and then pressed into pellets with 1.50 cm diameter using a uniaxial hydraulic press at 31 000 N. The pre-alloyed pellets were sintered at 1000 °C for 24 hours by using a Protherm PC442 tube furnace. Then checked *via* X-ray diffraction to ensure phase purity and that peaks remain narrow and intense. The geometrical density of the as-prepared pellets was in the 75–80% range. These pellets were then mixed into an isopropyl alcohol slurry and milled again into powder with yttrium-stabilized balls for 10 hours, then all the powder samples were dried in a fume hood at room temperature.

2.2. Materials characterization

The phase structure was characterized by the X-ray diffraction (XRD, Bruker D8 Advance X-ray diffractometer) at voltage of 40 kV and current of 50 mA under Cu Kα radiation (λ = 1.54178 Å), with a 1.5° min^{-1} of scan speed and a range taken as 2θ = 10–90°. Transmission electron microscopy (TEM) and scanning electron microscopy (SEM) images were acquired on JEM-1011 with the accelerating voltage of 200 kV and JEOL JSM-6700 M with the accelerating voltage of 10 kV, respectively. The sample for SEM

characterization was sputtered a thin layer of gold prior to the measurements. X-ray photoemission spectroscopy (XPS) was performed to determine the compositions and chemical states by using a Thermo Fisher X-ray photoelectron spectrometer ESCALAB 250Xi (non-monochromated Mg Kα X-ray radiation as the excitation source). The high-resolution transmission electron microscopy (HRTEM) images, selected area electron diffraction (SAED) pattern, and EDS elemental mapping images were obtained by using a JEM-ARM200F (Schottky FEG Cs corrected TEM). EDX analysis was carried out in the STEM mode using a Tecnai G2 F20 transmission electron microscope. The sample for TEM measurements was prepared by dispersing the $(Mg_{0.2}Ti_{0.2}Zn_{0.2}Cu_{0.2}Fe_{0.2})_3O_4$ nanoparticles into petroleum ether followed by dropping onto a gold grid. A Tristar II 3020 physisorption system (Micromeritics Instrument Corporation, USA) was used to measure nitrogen adsorption–desorption isotherms at the liquid nitrogen temperature (77 K). The Brunauer–Emmett–Teller (BET) method was used to calculate the specific surface areas of the samples from the adsorption branches. The Barrett–Joyner–Halenda (BJH) model was employed to compute pore size distribution curves from the desorption branches.

2.3. Electrochemical measurements

The working electrodes for LIBs were first fabricated by mixing active materials (submicrometer-sized $(Mg_{0.2}Ti_{0.2}Zn_{0.2}Cu_{0.2}Fe_{0.2})_3O_4$ particles), Super P acetylene black (20 wt%) and poly(vinylidene fluoride) (M_w: 534000 g mol^{-1}, Sigma-Aldrich) (10 wt%) using *N*-methyl pyrrolidone (NMP) as solvent to form a slurry with a weight ratio of 70 : 20 : 10. Then, the slurry was coated on Cu foil as current collector with a loading of 1.0 ± 0.2 mg cm^{-2}, dried in a vacuum oven at 80 °C overnight, and then roll-pressed at 10 MPa for 2 minutes. After that, the electrochemical properties were investigated using coin-type cells (CR2025), and the assembly process was operated in the Ar-filled glovebox with H_2O and O_2 contents less than 1.0 ppm. The electrolyte was adopted by dissolving 1.0 M $LiPF_6$ in ethylene carbonate/dimethyl carbonate (1/1 in volume), the counter electrode was lithium foil, and the separator was a Celgard 2400 microporous membrane. Cyclic voltammetry (CV) tests were carried out on the Autolab PGSTAT 302 N electrochemical station with a potential window of 0.01–3.0 V (*vs.* Li/Li^+) at various scan rates from 0.1 to 1.0 mV s^{-1}. Galvanostatic discharge/charge test (the mass loading of $(Mg_{0.2}Ti_{0.2}Zn_{0.2}Cu_{0.2}Fe_{0.2})_3O_4$ is about 1.2 mg) was conducted on a LAND CT2001A multichannel battery test system (LAND Technology Co., Ltd., China) at room temperature. The electrochemical workstation was also used to measure the electrochemical impedance spectroscopy (EIS) with the frequency range from 10^6 Hz to 0.01 Hz with alternating current signal amplitude of 10 mV.

3. Results and discussion

3.1. Structure characterization of the $(Mg_{0.2}Ti_{0.2}Zn_{0.2}Cu_{0.2}Fe_{0.2})_3O_4$ particles

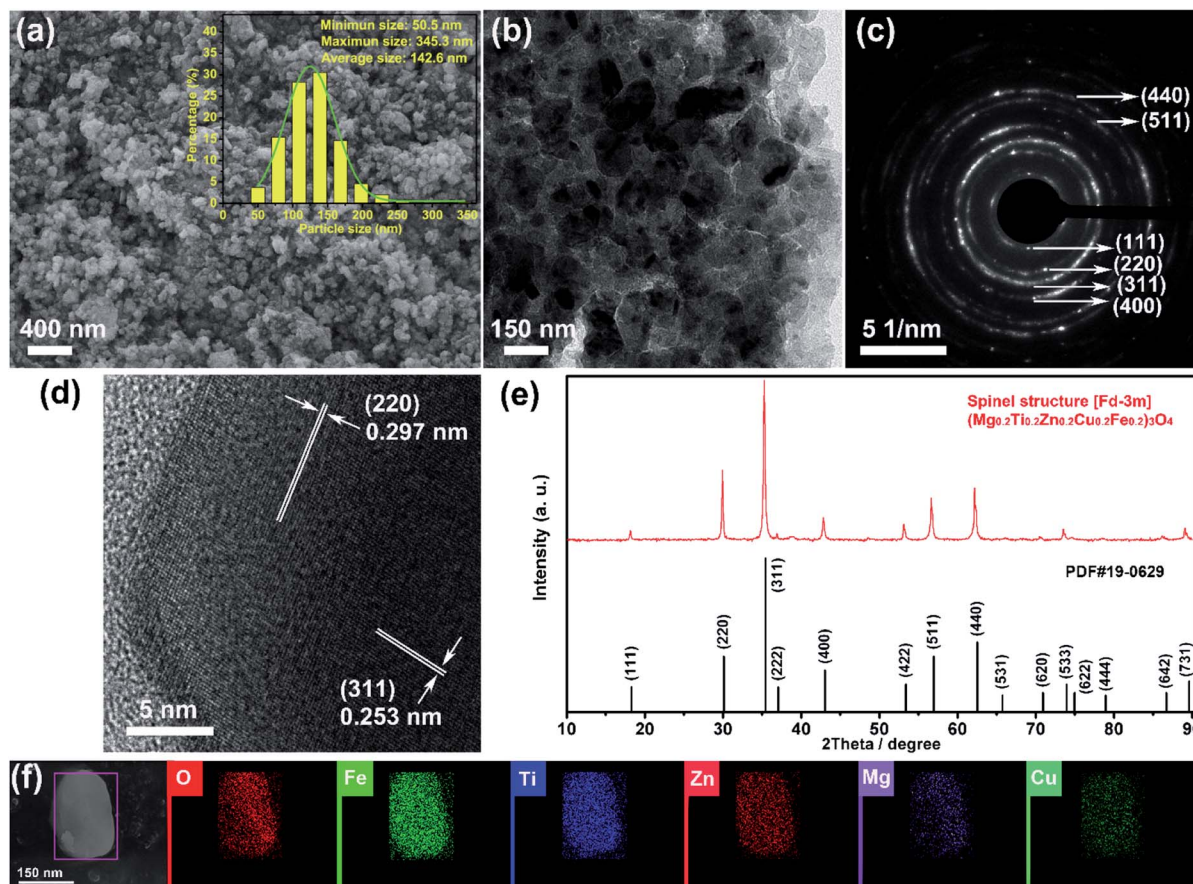Fig. 1(a) and (b) show the SEM and TEM images of the $(Mg_{0.2}Ti_{0.2}Zn_{0.2}Cu_{0.2}Fe_{0.2})_3O_4$ particles, which display irregular

Fig. 1 (a) SEM image and (b) TEM image of the synthesized irregular $(Mg_{0.2}Ti_{0.2}Zn_{0.2}Cu_{0.2}Fe_{0.2})_3O_4$ particles; (c) SAED pattern, (d) HR-TEM image, (e) XRD pattern and (f) elemental mapping images of the $(Mg_{0.2}Ti_{0.2}Zn_{0.2}Cu_{0.2}Fe_{0.2})_3O_4$ particles.

spherical morphology with size in the ranges of 51–345 nm (average size 143 nm). The XRD patterns of the $(Mg_{0.2}Ti_{0.2}Zn_{0.2}Cu_{0.2}Fe_{0.2})_3O_4$ particles are shown in Fig. 1(e) to investigate the crystal structure. The diffraction peaks at 2θ values of 18.21, 29.89, 35.26, 36.95, 42.79, 53.25, 56.64, 62.18, 73.56, and 89.09° correspond to the reflections of the (111), (220), (311), (222), (400), (422), (511), (440), (533), and (731) planes of a $Fd\bar{3}m$ spinel structure. Besides, no impurity peaks are detected, indicating the high purity of the spinel-structured materials. The polycrystalline diffraction rings of SAED pattern (as shown in Fig. 1(c)) present the microstructural characteristics of a typical face-centered-cubic (FCC) structure. The interplanar spacings (ring 1: d_{111} = 0.485 nm, ring 2: d_{220} = 0.297 nm, ring 3: d_{311} = 0.253 nm, ring 4: d_{400} = 0.209 nm, ring 5: d_{511} = 0.162 nm, and ring 6: d_{440} = 0.148 nm) are all assignable to the FCC structure. HRTEM image taken from an individual nanosheet (Fig. 1(d)) shows the well-defined lattice fringes with d spacing of 0.297 and 0.253 nm, which are in good agreement with the (220) and (311) planes of $(Mg_{0.2}Ti_{0.2}Zn_{0.2}Cu_{0.2}Fe_{0.2})_3O_4$ phase, respectively. It is clear that the corresponding interplanar spacing values agreed well with the SAED data. In order to confirm the element distribution of $(Mg_{0.2}Ti_{0.2}Zn_{0.2}Cu_{0.2}Fe_{0.2})_3O_4$ particles, EDS elemental mapping was performed (Fig. 1(f) and S1†), revealing that the Mg, Ti, Fe, Zn, Cu and O elements are homogeneously distributed within the region of a single particle with good overlapping.

It's well-known that the specific surface area, pore diameter, and pore volume all influence the electrochemical performance of the active electrode materials.[58–60] The specific surface area and pore size distribution of the synthesized $(Mg_{0.2}Ti_{0.2}Zn_{0.2}Cu_{0.2}Fe_{0.2})_3O_4$ particles were measured *via* nitrogen adsorption–desorption isotherm analysis (Fig. S2(a)†). The isotherm shows that the sample exhibits typical type-IV characteristics with a type-H1 hysteresis loop at high pressures, indicating the existence of open mesoporous characteristics.[61] According to the Brunauer–Emmett–Teller model, it presents a BET specific surface area of 12.31 m² g⁻¹, a Langmuir surface area of 78.21 m² g⁻¹, and a total pore volume of 0.037 cm³ g⁻¹. Pioneering research work of Fe_2O_3 by Reddy *et al.*[35,42] suggested that anode materials with a high BET surface area would be ideal choice (Table S1†). Based on Barrett–Joyner–Halenda plots, the pore size of the four samples is similar and mainly in the range of 3–20 nm (Fig. S2(b and c)†), which is strong evidence that the sample contain a large number of mesoporous structure. Generally, the rich mesoporous configuration would benefit for the long cycle lives and better rate capabilities of LIBs,[62] because such mesoporous structure possesses high specific surface area, which would facilitate charge transfer and reduce ion diffusion path lengths, and provide enough room for accommodating volume changes during cycling. To characterize the

chemical compositions and oxidation state of the $(Mg_{0.2}Ti_{0.2}Zn_{0.2}Cu_{0.2}Fe_{0.2})_3O_4$ particles, X-ray photoelectron spectroscopy (XPS) was performed. The XPS survey spectrum of the sample confirms the presence of Mg, Ti, Fe, Zn, Cu, and O elements in the material (Fig. S3†). Fig. S4(b)† shows that two main peaks are located at 231.9 and 235.1 eV in the Ti 2p XPS spectrum, corresponding to the Ti $2p_{3/2}$ and Ti $2p_{1/2}$ with oxidation state of Ti^{4+}.[63] In Fig. S4(c),† the O 1s peak is deconvoluted into two peaks. The peak around 529.5 eV arises from typical lattice O in $(Mg_{0.2}Ti_{0.2}Zn_{0.2}Cu_{0.2}Fe_{0.2})_3O_4$,[64] while the other peak centered at 531.5 eV is attributed to defect sites with low O atom harmonization. As shown in the high-resolution Fe 2p XPS spectrum of the $(Mg_{0.2}Ti_{0.2}Zn_{0.2}Cu_{0.2}Fe_{0.2})_3O_4$ particles (Fig. S4(d)†), two peaks centered at 710.8 and 724.1 eV are observed, corresponding to the electronic states of Fe $2p_{3/2}$ and Fe $2p_{1/2}$, respectively. Besides, the presences of two shake-up satellite peaks belong to the Fe^{3+}.[65,66] Two main peaks (Fig. S4(e)†) located at 933.3 and 953.5 eV in the Cu 2p XPS spectrum correspond to the Cu $2p_{3/2}$ and Cu $2p_{1/2}$ with oxidation state of Cu^{2+}, respectively. In Fig. S4(f),† the existence of Zn^{2+} species is demonstrated by strong peaks of Zn 2p centered at the binding energies of 1021.3 and 1044.5 eV, which can be ascribed to Zn $2p_{3/2}$ and Zn $2p_{1/2}$, respectively.

3.2. Electrochemical performance studies of the $(Mg_{0.2}Ti_{0.2}Zn_{0.2}Cu_{0.2}Fe_{0.2})_3O_4$ particles as anode material for LIBs

3.2.1. Cyclic voltammetry.
Cyclic voltammetry is a technique that is recognized as an efficient tool to study the redox reaction couples and structural transformations during Li-intercalation/deintercalation of both cathode[67,68] as well as anode materials.[12,69,70] Cyclic voltammetry (CV) studies on $(Mg_{0.2}Ti_{0.2}Zn_{0.2}Cu_{0.2}Fe_{0.2})_3O_4$ electrode were carried out at the scan rate of 0.2 mV s^{-1} in the voltage window of 0.01–3.0 V vs. Li/Li$^+$ at room temperature to study electron transfer kinetics and transport properties. Pure Li metal was used as the counter and reference electrode.

Fig. 2(a) shows the CV curves of the first seven cycles. It represents the first cathodic scan with four reduction peaks for $(Mg_{0.2}Ti_{0.2}Zn_{0.2}Cu_{0.2}Fe_{0.2})_3O_4$, in which the first one is centered at 1.42 V, the second one at 0.65 V, the third one at 0.35 V, which can apparently corresponding to the lithiation of Fe^{3+}/Fe^0, Cu^{2+}/Cu^0, Zn^{2+}/Zn^0, the Li_2O matrix formation and crystal structure destruction followed by Li-alloying of Zn, respectively.[71–73] The fourth sharp peak at lower voltage (0.03 V) can be ascribed to the formation of a solid electrolyte interphase (SEI) layer on the electrode surface because of the reduction of solvents in the electrolyte.[74,75]

Subsequently, the broad peak centered at around 1.41 V in the anodic step is identified due to oxidation of metallic Fe, Cu and Zn to the corresponding metal oxides, followed by the decomposition of Li_2O.[13,76] According to Wang et al.,[77] Li–Zn alloy formation occurs at 0.35 V and multistep dealloying process of Li–Zn alloy occurs in the range of 0.5–0.8 V vs. Li. As expected, three initial reduction peaks (1.42, 0.65 and 0.35 V) disappear, and the fourth one moves to 0.71 V in the second

cycle. Commonly, this phenomenon can be observed in transition metal oxides owing to some side reactions and structural rearrangements only happen in the first cycle, which indicates the irreversibility of initial lithiation process and the SEI formation.[13] In the following cycles, the CV curves are similar to the second cycle and almost are well-overlapped at 0.71 V and 1.41 V, suggesting the good electrochemical reversibility of the electrode.

3.2.2. Galvanostatic cycling studies.
In order to determine electrochemical properties of the $(Mg_{0.2}Ti_{0.2}Zn_{0.2}Cu_{0.2}Fe_{0.2})_3O_4$ electrode, galvanostatic cycling of the fabricated coin cells was done between 0.01 and 3.0 V vs. Li/Li$^+$, which was carried out on coin cells, up to 300 cycles at room temperature. The open-circuit voltage (OCV) of the fabricated and aged cells is about 2.8–3.0 V.

Fig. 2(b) summarizes the cyclic performance with coulombic efficiency of the $(Mg_{0.2}Ti_{0.2}Zn_{0.2}Cu_{0.2}Fe_{0.2})_3O_4$ electrode at a current density of 100 mA g^{-1}. As mentioned above, it is noticed that rapid capacity decay in the preliminary cycles because of complicated subsidiary reactions and irreversible structure transformation. Furthermore, the capacity values generally increase after specifically completing 50 cycles, which can be explained by the reversible formation/dissolution of polymeric gel-like film during the process of activation electrode materials for the transition metal oxide.[78] It can be observed in Fig. 2(c) that the $(Mg_{0.2}Ti_{0.2}Zn_{0.2}Cu_{0.2}Fe_{0.2})_3O_4$ electrode exhibit the first, second, 10th, 100th, 200th, and 300th charge/discharge curves at a current density of 100 mA g^{-1}. During the first cycle, the voltage dropped to a plateau of 1.42 V from the open circuit potential and then slowly decreased to 0.01 V. The initial discharge and charge capacities were 1261 and 634 mA h g^{-1}, corresponding to a low initial coulombic efficiency of 50.3%. However, the coulombic efficiency increased to about 99% after few initial cycles and maintained at this percentage for the entire test process. Finally, after 300 cycles, a high discharge specific capacity of 504 mA h g^{-1} was still maintained. The superior electrochemical cycling performance could be originated from the unique hierarchically assembled robust microspheres structure of the electrode after 1st discharge/charge cycle (Fig. S5†). On one hand, the well-connected microspheres can enhance the contact area between electrode and electrolyte, which facilitates to shorten the lithium ion diffusion length and accommodate the volume change during charge/discharge process. On the other hand, the spherical hierarchical morphology with low surface energy can alleviate the particle aggregation.[79]

3.2.3. Rate performance.
The rate properties of the $(Mg_{0.2}Ti_{0.2}Zn_{0.2}Cu_{0.2}Fe_{0.2})_3O_4$ electrode were displayed in Fig. 2(d). As the current density changed from 100 to 2000 mA g^{-1}, the specific capacities of 571, 460, 405, 342, and 268 mA h g^{-1} are correspondingly obtained. More significantly, when the current density is reverted to 100 mA g^{-1}, the electrode capacity is also regained to 552 mA h g^{-1} (Table S2†). Furthermore, the discharge–charge curves of $(Mg_{0.2}Ti_{0.2}Zn_{0.2}Cu_{0.2}Fe_{0.2})_3O_4$ at different current densities (Fig. 2(e)) show the similar and clear potential plateaus revealing the stable and superior rate properties. As Wang et al. suggested that the rate
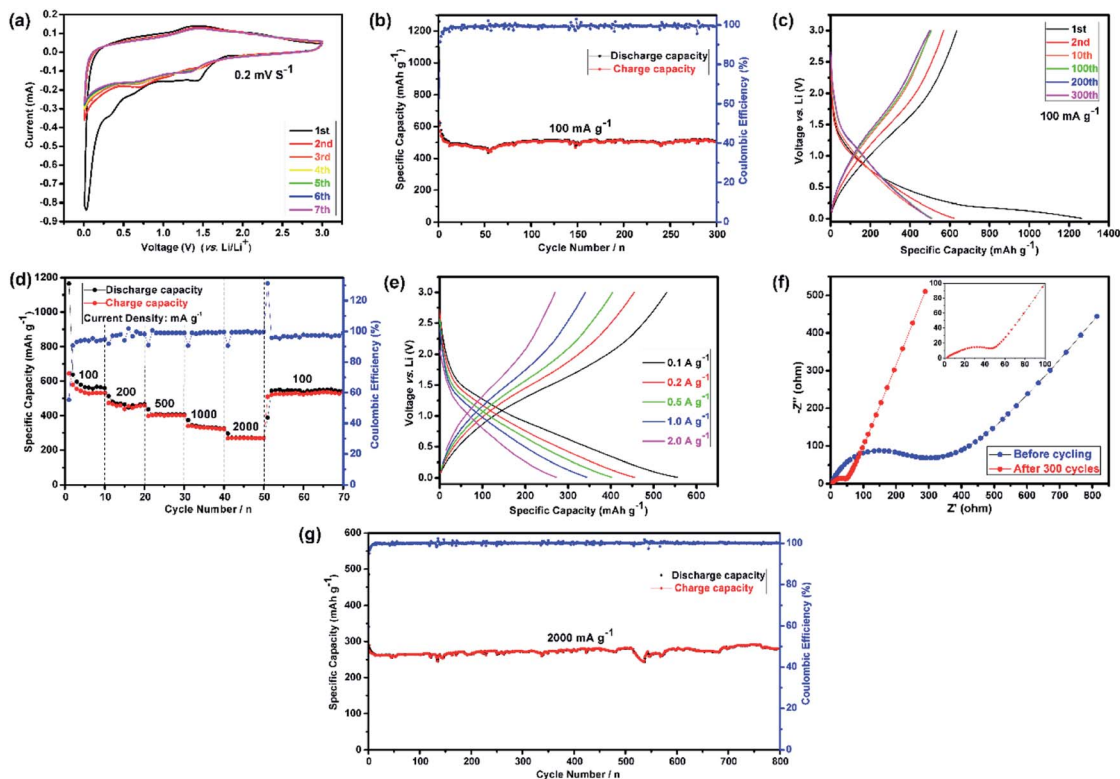
Fig. 2 Half-cell electrochemical performances of the $(Mg_{0.2}Ti_{0.2}Zn_{0.2}Cu_{0.2}Fe_{0.2})_3O_4$ electrode for LIBs. (a) Representative cyclic voltammetry (CV) curves at a scanning rate of 0.2 mV s^{-1} in the voltage range of 0.01–3.00 V *versus* Li$^+$/Li; (b) cycling performances and the corresponding coulombic efficiencies at 100 mA g^{-1} for 300 cycles; (c) discharge–charge voltage profiles for the 1st, 2nd, 10th, 100th, 200th and 300th cycles in the voltage range of 0.01–3.00 V at a current rate of 100 mA g^{-1}; (d) rate performance at different current densities ranging from 100 to 2000 mA g^{-1}; (e) the discharge–charge curves under different current densities; (f) Nyquist plots of the $(Mg_{0.2}Ti_{0.2}Zn_{0.2}Cu_{0.2}Fe_{0.2})_3O_4$ electrode: before cycling (at the open circuit voltage, 3.0 V) and after 300 cycles (at the specific charge voltage, 3.0 V) at a current density of 100 mA g^{-1}; (g) cycling performances and the corresponding coulombic efficiencies at 2000 mA g^{-1} for 800 cycles.

performance of electrode materials is extremely dependent on the electronic conductivity and diffusion path.[80] Introducing foreign atoms into the electrode material will increase the diffusion coefficient of Li ion (D_{Li^+}). Thus, the rational design and selection of $(Mg_{0.2}Ti_{0.2}Zn_{0.2}Cu_{0.2}Fe_{0.2})_3O_4$ as anode material will lead to greater electronic conductivity and multiple electrochemically active components as compared with the single metal oxides. Notably, at the elevated current density long-term cyclic evaluation under 2000 mA g^{-1} (Fig. 2(g)), it displays the robust cyclic stability (no obvious capacity fading and close to 100% coulombic efficiency) and maintains on 279 mA h g^{-1} at the end of 800 cycles. The excellent long-term cycling performance would be ascribed to the property of high entropy oxides, which not only have robust structural stability, but also with enhanced electronic conductivity.

3.2.4. Electrochemical impedance spectroscopy. Electrochemical impedance spectroscopy (EIS) is one of the most informative analytical techniques that can be employed to understand reaction kinetics of the Li-ion insertion/deinsertion process in compounds due to its nondestructive nature and ability to differentiate various phenomena taking place in an electrode at different time periods.[71,81,82]

Presently, to investigate the electrical conductivity and Li$^+$ transfer in the $(Mg_{0.2}Ti_{0.2}Zn_{0.2}Cu_{0.2}Fe_{0.2})_3O_4$ anode, EIS plots of before cycling (at the open circuit voltage, 3.0 V) and after 300 cycles (at the specific charge voltage, 3.0 V) were evaluated. As shown in Fig. 2(f), the Nyquist plots show a semicircle in the high-to middle-frequency region (representing the ohmic resistance, SEI film resistance, and charge transfer resistance) and a straight sloping line in the low-frequency region (representing Li$^+$ diffusion resistance).[83,84] It is noted that the semicircle diameter of the fresh $(Mg_{0.2}Ti_{0.2}Zn_{0.2}Cu_{0.2}Fe_{0.2})_3O_4$ electrode is larger than that measured at the 300th cycle, indicating that the Li$^+$ diffusion resistance is reduced after cycling. The semicircle diameter varies directly with impedance. The impedance data of all samples are analyzed by fitting the equivalent circuits inserted in Fig. 3. The equivalent circuits are composed of ohmic resistance (R_S), SEI film resistance (R_{SEI}), charge-transfer resistance (R_{ct}), constant-phase element (CPE), and Warburg impedance (Z_W). The parameters of the equivalent circuit are recorded in Table S3.† In this way, $(Mg_{0.2}Ti_{0.2}Zn_{0.2}Cu_{0.2}Fe_{0.2})_3O_4$ exhibits excellent electrical conductivity. Fig. 3 shows the relationship between the real resistance (Z') and the inverse square root of frequency ($\omega^{-1/2}$) of the $(Mg_{0.2}Ti_{0.2}Zn_{0.2}Cu_{0.2}Fe_{0.2})_3O_4$ electrode before and after 300 cycles. The
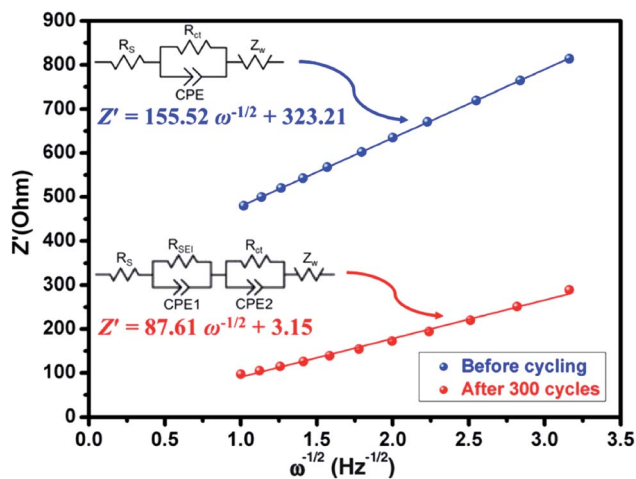
Fig. 3 Plots of Z' against $\omega^{-1/2}$ (inset: equivalent circuit) of the fresh $(Mg_{0.2}Ti_{0.2}Zn_{0.2}Cu_{0.2}Fe_{0.2})_3O_4$ half-cell and the half-cell charged to 3.0 V after 300 cycles.

diffusion coefficient values of Li^+ into the electrodes can be calculated by the following equations:[85,86]

$$D_{Li^+} = \frac{R^2 T^2}{2A^2 n^4 F^4 C^2 \sigma^2}$$

$$Z' = R_S + R_{ct} + \sigma\omega^{-1/2}$$

where R is the gas constant (8.3145 J mol^{-1} K^{-1}), T is the test temperature (298.15 K), A is the surface area of the electrode (1.76625 cm^2), n is the number of electrons per molecule during oxidization (which, in this case, n = 4.2), F is the Faraday constant (96 485.33 C mol^{-1}), C is the concentration of lithium ion, and σ is the Warburg factor, which is related to Z'. The $(Mg_{0.2}Ti_{0.2}Zn_{0.2}Cu_{0.2}Fe_{0.2})_3O_4$ electrode after 300 cycles shows the Li^+ diffusion coefficient of 4.716×10^{-15} cm^2 s^{-1}, 3.15 times higher than that of the fresh cell (1.497×10^{-15} cm^2 s^{-1}), explaining the good electrochemical performance. Hence, we believe that the $(Mg_{0.2}Ti_{0.2}Zn_{0.2}Cu_{0.2}Fe_{0.2})_3O_4$ material show higher electrical conductivity because of the five types of metals in the spinel structure, which reduce the activation energy for electron transfer relative to that in single-metal structures.

3.2.5. Investigation on the kinetics origin of the $(Mg_{0.2}Ti_{0.2}Zn_{0.2}Cu_{0.2}Fe_{0.2})_3O_4$ electrode. The broad redox peaks observed and the quasilinear charge curves from the CV and charge/discharge profiles, respectively, suggest the pseudocapacitive properties of the $(Mg_{0.2}Ti_{0.2}Zn_{0.2}Cu_{0.2}Fe_{0.2})_3O_4$ electrode. It is well-known that the peak current values in CV curves for the cathodic and anodic reactions would vary with scan rate, which could imply the kinetics of the lithium insertion/extraction at the electrode/electrolyte interface. Hence, in order to better understanding the kinetics mechanism, CV measurements were conducted at various scan rates from 0.1 to 1.0 mV s^{-1} to investigate the kinetics of lithium uptake within the $(Mg_{0.2}Ti_{0.2}Zn_{0.2}Cu_{0.2}Fe_{0.2})_3O_4$ electrode, as shown in Fig. 4.

It is presented in Fig. 4(a) that two anodic peaks and one cathodic peak can be observed at various scan rates. The logarithm of the peak current (i_p) is plotted versus the logarithm of the scan rate (v) (Fig. 4(b)), assuming that i_p and v obey the power-law relationship as the following two equations:[87,88]

$$i_p = av^b$$

$$\log(i_p) = b\log(v) + \log a$$

where a and b are adjustable values. The value of b offers insight into the charge-storage mechanism. By plotting $\log(i_p)$ against $\log(v)$, the b value can be derived from the slope, which gives two critical conditions: $b = 0.5$ and $b = 1.0$. It is suggested by many references that former indicates a typical faradaic intercalation process controlled by semi-infinite linear diffusion; the latter represents surface capacitive charge storage free of diffusion control.[89,90] As shown in Fig. 4(b), the slopes (b value) of the three peaks are calculated to be 0.97, 0.86 and 0.90, respectively, demonstrating that the behavior of lithium storage in $(Mg_{0.2}Ti_{0.2}Zn_{0.2}Cu_{0.2}Fe_{0.2})_3O_4$ electrode is mainly controlled by the surface redox reaction process.

The total capacitive contribution at a fixed scan rate can be quantitatively determined according to the following equation:

$$i(V) = k_1 v + k_2 v^{1/2}$$

where the k_1 and k_2 values are constants at a particular voltage. $k_1 v$ stands for the capacitive-controlled contribution and $k_2 v^{1/2}$ represents the diffusion-controlled contribution, respectively, where v is the scan rate. For convenient analytical purposes, we can rearrange this equation slightly to:

$$i(V)/v^{1/2} = k_1 v^{1/2} + k_2$$

Thus, by determining k_1 and k_2 in Fig. S6,† we are able to quantify the fraction of the current due to each of these contributions at specific potentials. It presents that when increasing the scan rates, the capacitive contribution also increased (Fig. 4(d)). The blue areas in the CV curve shown in Fig. 4(c) represent the capacitive-controlled contribution at a scan rate of 1.0 mV s^{-1}. Fig. S7† shows the CV curves with separation between the total current and surface capacitive current at different scan rates of the $(Mg_{0.2}Ti_{0.2}Zn_{0.2}Cu_{0.2}Fe_{0.2})_3O_4$ electrode. At the scan rate of 0.1 mV s^{-1}, the capacitive contribution is 62.9%; a high ratio of 93.2% can be obtained when the scan rate approaches 1.0 mV s^{-1}. The dominant pseudocapacitive contribution indicates the superior rate capability, and associates with the structure of the $(Mg_{0.2}Ti_{0.2}Zn_{0.2}Cu_{0.2}Fe_{0.2})_3O_4$ materials, in which the lithium ions can directly react with the active material without long distance diffusion pathways.

4. Conclusions

In this study, we have demonstrated the successful preparation of a new kind of spinel high-entropy oxide
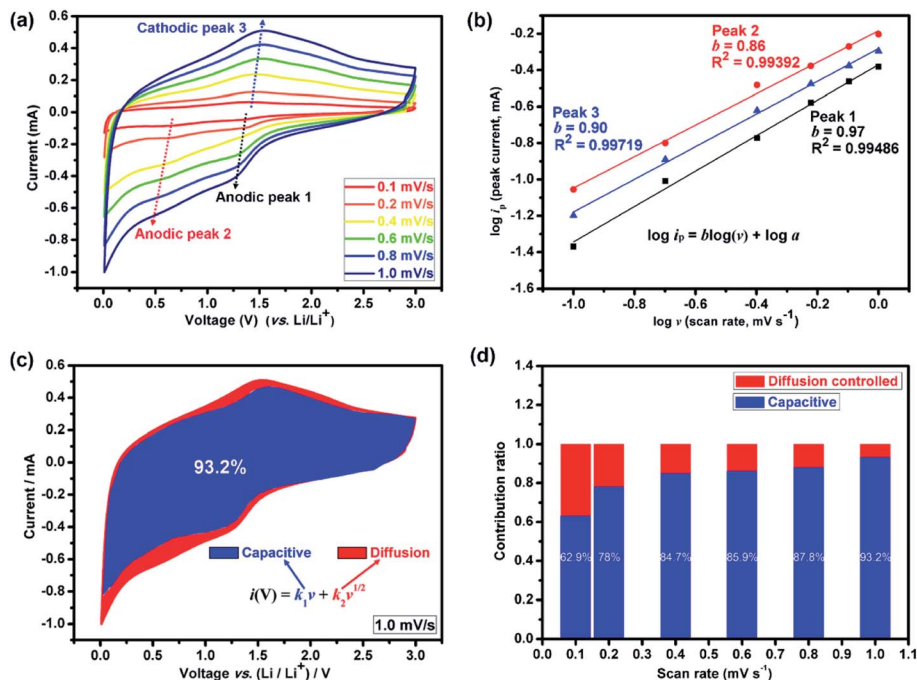
Fig. 4 Kinetic analysis of the Li$^+$ storage behavior. (a) Cyclic voltammetry (CV) curves of the $(Mg_{0.2}Ti_{0.2}Zn_{0.2}Cu_{0.2}Fe_{0.2})_3O_4$ electrode for LIBs at different scan rates of 0.1, 0.2, 0.4, 0.6, 0.8 and 1.0 mV s^{-1}. (b) The corresponding logarithm peak current *versus* logarithm scan rate plots with inset showing the calculated *b* values. (c) Separation of capacitive (blue region) and diffusion (red region) controlled contribution at 1.0 mV s^{-1}. (d) The normalized contribution ratio of pseudocapacitive capacities at different scan rates for the $(Mg_{0.2}Ti_{0.2}Zn_{0.2}Cu_{0.2}Fe_{0.2})_3O_4$ electrode, which indicates that the electrode was mainly controlled by pseudocapacitive electrochemical behavior.

$(Mg_{0.2}Ti_{0.2}Zn_{0.2}Cu_{0.2}Fe_{0.2})_3O_4$ material *via* a facile one-step solid state reaction method and subsequently high-energy ball-milling. When used as anode materials for LIBs, the electrode exhibited superior lithium storage properties, delivering a large reversible capacity of 504 mA h g^{-1} at a current density of 100 mA g^{-1} after 300 cycles, and notably an exceptional rate capacity of 272 mA h g^{-1} at 2000 mA g^{-1}, respectively. Meanwhile, a high capacity retention of 96.2% after 800 cycles at 2000 mA g^{-1} was obtained. This superior electrochemical performance could be ascribed to the usage of novel $(Mg_{0.2}\-Ti_{0.2}Zn_{0.2}Cu_{0.2}Fe_{0.2})_3O_4$ particle structure, which can not only buffer the volumetric changes upon lithiation/delithiation processes, but also provide enlarged surface sites for lithium storage and facilitate the charge/electrolyte reaction. More importantly, our work highlights that the rational design and use of high-entropy oxides with different electrochemically active elements and novel structure as LIB anode materials might be promising for exploring next-generation energy storage devices.

Conflicts of interest

There are no conflicts to declare.

Acknowledgements

Notes and references

1 J. M. Tarascon and M. Armand, *Nature*, 2001, **414**, 359–367.
2 N. J. Dudney and J. Li, *Science*, 2015, **347**, 131.
3 P. Poizot, S. Laruelle, S. Grugeon, L. Dupont and J. M. Tarascon, *Nature*, 2000, **407**, 496–499.
4 D. Xiong, X. Li, Z. Bai and S. Lu, *Small*, 2018, **14**, 1703419.
5 W. Liu, X. Li, D. Xiong, Y. Hao, J. Li, H. Kou, B. Yan, D. Li, S. Lu, A. Koo, K. Adair and X. Sun, *Nano Energy*, 2018, **44**, 111–120.
6 P. G. Bruce, B. Scrosati and J.-M. Tarascon, *Angew. Chem., Int. Ed.*, 2008, **47**, 2930–2946.
7 J. B. Goodenough and K.-S. Park, *J. Am. Chem. Soc.*, 2013, **135**, 1167–1176.
8 H. Wang, X. Yang, Q. Wu, Q. Zhang, H. Chen, H. Jing, J. Wang, S.-B. Mi, A. L. Rogach and C. Niu, *ACS Nano*, 2018, **12**, 3406–3416.
9 S. Lim, J.-H. Kim, Y. Yamada, H. Munakata, Y.-S. Lee, S.-S. Kim and K. Kanamura, *J. Power Sources*, 2017, **355**, 164–170.
10 E. Yoo, J. Kim, E. Hosono, H.-s. Zhou, T. Kudo and I. Honma, *Nano Lett.*, 2008, **8**, 2277–2282.

11 J. Wang, H. Wang, D. Cao, X. Lu, X. Han and C. Niu, *Part. Part. Syst. Charact.*, 2017, **34**, 1700185.

12 M. V. Reddy, G. V. Subba Rao and B. V. Chowdari, *Chem. Rev.*, 2013, **113**, 5364–5457.

13 K. Cao, T. Jin, L. Yang and L. Jiao, *Mater. Chem. Front.*, 2017, **1**, 2213–2242.

14 L. Fan, X. Li, X. Song, N. Hu, D. Xiong, A. Koo and X. Sun, *ACS Appl. Mater. Interfaces*, 2018, **10**, 2637–2648.

15 M. V. Reddy, G. Prithvi, K. P. Loh and B. V. R. Chowdari, *ACS Appl. Mater. Interfaces*, 2014, **6**, 680–690.

16 L. Wang, G. Zhang, Q. Liu and H. Duan, *Mater. Chem. Front.*, 2018, **2**, 1414–1435.

17 H. Zhang, G. Zhang, Z. Li, K. Qu, L. Wang, W. Zeng, Q. Zhang and H. Duan, *J. Mater. Chem. A*, 2016, **4**, 10585–10592.

18 Q. Zhang, J. Wang, D. Xu, Z. Wang, X. Li and K. Zhang, *J. Mater. Chem. A*, 2014, **2**, 3865–3874.

19 Q. Zhang, D. Xu, X. Zhou, X. Wu and K. Zhang, *Small*, 2014, **10**, 935–943.

20 H. Huang, Y. Liu, J. Wang, M. Gao, X. Peng and Z. Ye, *Nanoscale*, 2013, **5**, 1785–1788.

21 M. V. Reddy, C. Yu, F. Jiahuan, K. P. Loh and B. V. R. Chowdari, *ACS Appl. Mater. Interfaces*, 2013, **5**, 4361–4366.

22 F.-X. Ma, H. Hu, H. B. Wu, C.-Y. Xu, Z. Xu, L. Zhen and X. W. Lou, *Adv. Mater.*, 2015, **27**, 4097–4101.

23 S. H. Lee, S.-H. Yu, J. E. Lee, A. Jin, D. J. Lee, N. Lee, H. Jo, K. Shin, T.-Y. Ahn, Y.-W. Kim, H. Choe, Y.-E. Sung and T. Hyeon, *Nano Lett.*, 2013, **13**, 4249–4256.

24 B. Wang, H. B. Wu, L. Zhang and X. W. Lou, *Angew. Chem., Int. Ed.*, 2013, **52**, 4165–4168.

25 S. Petnikota, S. K. Marka, A. Banerjee, M. V. Reddy, V. V. S. S. Srikanth and B. V. R. Chowdari, *J. Power Sources*, 2015, **293**, 253–263.

26 J. Wang, H. Zhou, J. Nanda and P. V. Braun, *Chem. Mater.*, 2015, **27**, 2803–2811.

27 L. Zhang, H. B. Wu, R. Xu and X. W. Lou, *CrystEngComm*, 2013, **15**, 9332–9335.

28 J. Liang, Z. Fan, S. Chen, S. Ding and G. Yang, *Chem. Mater.*, 2014, **26**, 4354–4360.

29 Y. Chen, Y. Wang, X. Shen, R. Cai, H. Yang, K. Xu, A. Yuan and Z. Ji, *J. Mater. Chem. A*, 2018, **6**, 1048–1056.

30 M. V. Reddy, Z. Beichen, L. J. e. Nicholette, Z. Kaimeng and B. V. R. Chowdari, *Electrochem. Solid-State Lett.*, 2011, **14**, A79–A82.

31 M. V. Reddy, K. Y. H. Kenrick, T. Y. Wei, G. Y. Chong, G. H. Leong and B. V. R. Chowdari, *J. Electrochem. Soc.*, 2011, **158**, A1423–A1430.

32 M. V. Reddy, C. Yu, F. Jiahuan, K. P. Loh and B. V. R. Chowdari, *RSC Adv.*, 2012, **2**, 9619–9625.

33 B. Das, M. V. Reddy and B. V. R. Chowdari, *J. Alloys Compd.*, 2013, **565**, 90–96.

34 M. V. Reddy, Y. Xu, V. Rajarajan, T. Ouyang and B. V. R. Chowdari, *ACS Sustainable Chem. Eng.*, 2015, **3**, 3035–3042.

35 M. V. Reddy, C. T. Cherian, K. Ramanathan, K. C. W. Jie, T. Y. W. Daryl, T. Y. Hao, S. Adams, K. P. Loh and B. V. R. Chowdari, *Electrochim. Acta*, 2014, **118**, 75–80.

36 Y. Wu, P. Zhu, M. V. Reddy, B. V. R. Chowdari and S. Ramakrishna, *ACS Appl. Mater. Interfaces*, 2014, **6**, 1951–1958.

37 D. Darbar, M. V. Reddy, S. Sundarrajan, R. Pattabiraman, S. Ramakrishna and B. V. R. Chowdari, *Mater. Res. Bull.*, 2016, **73**, 369–376.

38 C. T. Cherian, J. Sundaramurthy, M. V. Reddy, P. Suresh Kumar, K. Mani, D. Pliszka, C. H. Sow, S. Ramakrishna and B. V. R. Chowdari, *ACS Appl. Mater. Interfaces*, 2013, **5**, 9957–9963.

39 D. Darbar, M. R. Anilkumar, V. Rajagopalan, I. Bhattacharya, H. I. Elim, T. Ramakrishnappa, F. I. Ezema, R. Jose and M. V. Reddy, *Ceram. Int.*, 2018, **44**, 4630–4639.

40 M. V. Reddy, C. Yao Quan and S. Adams, *Mater. Lett.*, 2018, **212**, 186–192.

41 C. T. Cherian, M. V. Reddy, G. V. S. Rao, C. H. Sow and B. V. R. Chowdari, *J. Solid State Electrochem.*, 2012, **16**, 1823–1832.

42 M. V. Reddy, C. Y. Quan, K. W. Teo, L. J. Ho and B. V. R. Chowdari, *J. Phys. Chem. C*, 2015, **119**, 4709–4718.

43 J. Zhao, Y. Cheng, X. Yan, D. Sun, F. Zhu and Q. Xue, *CrystEngComm*, 2012, **14**, 5879–5885.

44 L. Luo, R. Cui, H. Qiao, K. Chen, Y. Fei, D. Li, Z. Pang, K. Liu and Q. Wei, *Electrochim. Acta*, 2014, **144**, 85–91.

45 L. Jin, Y. Qiu, H. Deng, W. Li, H. Li and S. Yang, *Electrochim. Acta*, 2011, **56**, 9127–9132.

46 Y. Yin, N. Huo, W. Liu, Z. Shi, Q. Wang, Y. Ding, J. Zhang and S. Yang, *Scr. Mater.*, 2016, **110**, 92–95.

47 Y. Yin, W. Liu, R. Gao and S. Yang, *ChemElectroChem*, 2019, **6**, 757–763.

48 A. K. Rai, T. V. Thi, J. Gim and J. Kim, *Mater. Charact.*, 2014, **95**, 259–265.

49 X. Xu, C. Niu, M. Duan, X. Wang, L. Huang, J. Wang, L. Pu, W. Ren, C. Shi, J. Meng, B. Song and L. Mai, *Nat. Commun.*, 2017, **8**, 460.

50 C. Liu, F. Li, L.-P. Ma and H.-M. Cheng, *Adv. Mater.*, 2010, **22**, E28–E62.

51 D. W. Kim, Y. D. Ko, J. G. Park and B. K. Kim, *Angew. Chem., Int. Ed.*, 2007, **46**, 6654–6657.

52 N. Prasoetsopha, S. Pinitsoontorn, S. Fan, H. H. Hng and S. Maensiri, *Ionics*, 2017, **23**, 395–403.

53 A. Sarkar, L. Velasco, D. Wang, Q. Wang, G. Talasila, L. de Biasi, C. Kübel, T. Brezesinski, S. S. Bhattacharya, H. Hahn and B. Breitung, *Nat. Commun.*, 2018, **9**, 3400.

54 A. Sarkar, Q. Wang, A. Schiele, M. R. Chellali, S. S. Bhattacharya, D. Wang, T. Brezesinski, H. Hahn, L. Velasco and B. Breitung, *Adv. Mater.*, 2019, 1806236.

55 Q. Wang, A. Sarkar, Z. Li, Y. Lu, L. Velasco, S. S. Bhattacharya, T. Brezesinski, H. Hahn and B. Breitung, *Electrochem. Commun.*, 2019, **100**, 121–125.

56 Q. Wang, A. Sarkar, D. Wang, L. Velasco, R. Azmi, S. S. Bhattacharya, T. Bergfeldt, A. Düvel, P. Heitjans, T. Brezesinski, H. Hahn and B. Breitung, *Energy Environ. Sci.*, 2019, **12**, 2433–2442.

57 N. Qiu, H. Chen, Z. Yang, S. Sun, Y. Wang and Y. Cui, *J. Alloys Compd.*, 2019, **777**, 767–774.

58 H. Chen, N. Qiu, B. Wu, Z. Yang, S. Sun and Y. Wang, *RSC Adv.*, 2019, **9**, 28908–28915.

59 W. Cheng, F. Rechberger, D. Primc and M. Niederberger, *Nanoscale*, 2015, **7**, 13898–13906.

60 H. Li, P. Zhou, F. Liu, H. Li, F. Cheng and J. Chen, *Chem. Sci.*, 2019, **10**, 1374–1379.

61 K. Zhu, H. Gao, G. Hu, M. Liu and H. Wang, *J. Power Sources*, 2017, **340**, 263–272.

62 F. Zou, X. Hu, Z. Li, L. Qie, C. Hu, R. Zeng, Y. Jiang and Y. Huang, *Adv. Mater.*, 2014, **26**, 6622–6628.

63 P. Zhu, Y. Wu, M. V. Reddy, A. Sreekumaran Nair, B. V. R. Chowdari and S. Ramakrishna, *RSC Adv.*, 2012, **2**, 531–537.

64 L. Qu, X. Hou, J. Mao, Q. Ru, S. Hu, X. Liu and K.-h. Lam, *RSC Adv.*, 2016, **6**, 96743–96751.

65 M. C. Biesinger, B. P. Payne, A. P. Grosvenor, L. W. M. Lau, A. R. Gerson and R. S. C. Smart, *Appl. Surf. Sci.*, 2011, **257**, 2717–2730.

66 I. Uhlig, R. Szargan, H. W. Nesbitt and K. Laajalehto, *Appl. Surf. Sci.*, 2001, **179**, 222–229.

67 M. V. Reddy, G. V. Subba Rao and B. V. R. Chowdari, *Electrochim. Acta*, 2005, **50**, 3375–3382.

68 S. L. Tey, M. V. Reddy, G. V. Subba Rao, B. V. R. Chowdari, J. Yi, J. Ding and J. J. Vittal, *Chem. Mater.*, 2006, **18**, 1587–1594.

69 M. V. Reddy, B. Pecquenard, P. Vinatier and A. Levasseur, *Electrochem. Commun.*, 2007, **9**, 409–415.

70 B. Varghese, M. V. Reddy, Z. Yanwu, C. S. Lit, T. C. Hoong, G. V. Subba Rao, B. V. R. Chowdari, A. T. S. Wee, C. T. Lim and C.-H. Sow, *Chem. Mater.*, 2008, **20**, 3360–3367.

71 M. V. Reddy, B. L. Wei Wen, K. P. Loh and B. V. R. Chowdari, *ACS Appl. Mater. Interfaces*, 2013, **5**, 7777–7785.

72 C. T. Cherian, M. Zheng, M. V. Reddy, B. V. R. Chowdari and C. H. Sow, *ACS Appl. Mater. Interfaces*, 2013, **5**, 6054–6060.

73 M. V. Reddy, G. V. Subba Rao and B. V. R. Chowdari, *J. Mater. Chem.*, 2011, **21**, 10003–10011.

74 Y. Gao, L. Yin, S. J. Kim, H. Yang, I. Jeon, J.-P. Kim, S. Y. Jeong, H. W. Lee and C. R. Cho, *Electrochim. Acta*, 2019, **296**, 565–574.

75 L. Hou, R. Bao, Y. Zhang, X. Sun, J. Zhang, H. Dou, X. Zhang and C. Yuan, *J. Mater. Chem. A*, 2018, **6**, 17947–17958.

76 Y. Deng, Q. Zhang, S. Tang, L. Zhang, S. Deng, Z. Shi and G. Chen, *Chem. Commun.*, 2011, **47**, 6828–6830.

77 H. Wang, Q. Pan, Y. Cheng, J. Zhao and G. Yin, *Electrochim. Acta*, 2009, **54**, 2851–2855.

78 P. F. Teh, Y. Sharma, S. S. Pramana and M. Srinivasan, *J. Mater. Chem.*, 2011, **21**, 14999–15008.

79 L. Hu, H. Zhong, X. Zheng, Y. Huang, P. Zhang and Q. Chen, *Sci. Rep.*, 2012, **2**, 986.

80 J. Wang, S. Xie, T. Liu, T. Yao, L. Zhu, A. M. Asiri, H. M. Marwani, X. Han and H. Wang, *Mater. Today Commun.*, 2019, **20**, 100578.

81 P. Nithyadharseni, M. V. Reddy, B. Nalini, M. Kalpana and B. V. R. Chowdari, *Electrochim. Acta*, 2015, **161**, 261–268.

82 M. V. Reddy, G. V. Subba Rao and B. V. R. Chowdari, *J. Phys. Chem. C*, 2007, **111**, 11712–11720.

83 A. K. Rai, S. Kim, J. Gim, M. H. Alfaruqi, V. Mathew and J. Kim, *RSC Adv.*, 2014, **4**, 47087–47095.

84 L. Hou, L. Lian, L. Zhang, G. Pang, C. Yuan and X. Zhang, *Adv. Funct. Mater.*, 2015, **25**, 238–246.

85 G. Li, X. Xu, R. Han and J. Ma, *CrystEngComm*, 2016, **18**, 2949–2955.

86 J. Zhu, L. Wei, J. Hu and C. Xue, *J. Alloys Compd.*, 2017, **723**, 729–735.

87 V. Augustyn, P. Simon and B. Dunn, *Energy Environ. Sci.*, 2014, **7**, 1597–1614.

88 J. Wang, J. Polleux, J. Lim and B. Dunn, *J. Phys. Chem. C*, 2007, **111**, 14925–14931.

89 V. Augustyn, J. Come, M. A. Lowe, J. W. Kim, P.-L. Taberna, S. H. Tolbert, H. D. Abruña, P. Simon and B. Dunn, *Nat. Mater.*, 2013, **12**, 518.

90 L. Shen, H. Lv, S. Chen, P. Kopold, P. A. van Aken, X. Wu, J. Maier and Y. Yu, *Adv. Mater.*, 2017, **29**, 1700142.